

Trajectory Generation of FBG-Sensorized Needles for Insertions into Multi-Layer Tissue

Dimitri A. Lezcano, Iulian I. Iordachita, Jin Seob Kim,
Department of Mechanical Engineering, Johns Hopkins University, Baltimore, MD, USA
Email: {dlezcan1, iordachita, jkim115}@jhu.edu

Abstract—Several models incorporate needle shape prediction, however prediction in multi-layer tissue for complex needle shape remains an issue. In this work, we present a method for trajectory generation of flexible needles that allows for complex curvatures, extending upon a previous sensor-based model. This model combines curvature measurements from fiber Bragg grating (FBG) sensors and the mechanics of an inextensible elastic rod for shape-sensing. We evaluate the method's effectiveness in single- and double-layer isotropic tissue prediction. The results illustrate a valid trajectory generation method accounting for complex curvatures in flexible needles.

Index Terms—flexible needle; FBG; mathematical model; tissue inhomogeneity; needle motion planning;

I. INTRODUCTION

Since the pioneering work of unicycle/bicycle model [1], [2], there have been many good models applied to flexible needle steering. The different kinds of models include kinematics-based models [1]–[3] and mechanics-based models [4]–[6]. Kinematics-based models have been used in control and planning of the needle, but may not properly capture additional or complex needle deformation. Mechanics-based models are usually based on classical beam theory to determine needle shape, but require detailed information on the tissue. During prostate surgery, for example, accurate needle placement through insertion into multi-layer tissue is required to prohibit from significant tissue damage. A sensor-based model using a Lie-group theoretic approach [7] has been proven successful for shape-sensing in multi-layer tissue using FBG sensors [8]. This model is based on the theory of elastic rods and Lie groups with the advantage of complex needle shape recognition in 3D space through the use of FBG sensors.

Aside from needle shape-sensing, an important issue to transition into human tissue is the prediction of needle shape during insertion in multi-layer tissue. Prediction of needle insertion is directly performed in kinematics-based models by integrating the system equation, however, the model that we apply treats the needle as a loaded elastic rod, requiring special consideration. In this paper, we propose and evaluate our needle insertion prediction model, expanding upon [7], [8], for single- and double-layer insertion scenarios. Specifically, we investigate necessary factors of the model that are influenced by increasing insertion lengths. To do that, we model uniformly-distributed loading conditions over increased

lengths of an elastic rod in order to determine proper scaling parameters in needle curvatures. Amidst the COVID-19 pandemic, we rely upon previous data presented in [7] to perform our prediction optimization in real data for single- and double-layer insertion scenarios. In Section II and III, the model and the simulations are explained. After the simulation results in Section IV, we conclude the paper.

II. THE MATHEMATICAL MODEL

A. Needle Shape-Sensing

The sensor-based model (see [7] for the details) describes the curvature (ω_1 and ω_2 along the local x - and y -axes, respectively) and torsion (ω_3 along the local z -axis) of the needle as

$$\omega(s) = [\omega_1 \ \omega_2 \ \omega_3]^T = \left(R^T(s) \frac{dR(s)}{ds} \right)^\vee \quad (1)$$

where $R(s) \in SO(3)$ denotes the rotation matrix in 3D space describing the orientation of the body-fixed frame attached at each point along the needle. $s \in [0, L]$ denotes the arclength of the needle with total insertion length L . Here \vee operation defines a 3D vector associated with a 3×3 skew-symmetric matrix $R^T \frac{dR}{ds}$ [9].

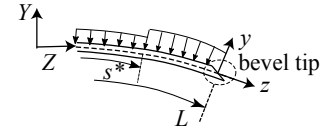


Fig. 1: A schematic of the bevel-tipped needle in the ideal insertion into two-layered tissue, which is modeled as two different uniformly distributed loads (normal components are only shown).

When inserting into tissue, the needle is modeled as an inextensible elastic rod. Under ideal conditions, we assume that the needle experiences uniformly distributed loads. In case of homogeneous tissue (i.e., single-layer) insertion, a single uniformly-distributed load and for two-layered tissue, two different, uniformly-distributed loads are assumed. In all cases, due to an asymmetric bevel tip, the needle deforms only in one plane (yz plane in the world frame), which is captured by introducing the intrinsic curvature $\kappa_0(s)$. For the single- and double-layer cases, they both introduce κ_c constants, denoted as intrinsic curvature constants. Refer to [7] for details. Then, through the minimization of the elastic potential energy in the

This work has been supported by the National Institutes of Health under grant No. R01CA235134.

rod using the Euler-Poincaré (E-P) equation [10], [11] together with FBG sensor data, we determine the deformation, $\omega(s)$, and subsequently, $\mathbf{r}(s)$, the points along the needle.

B. Needle Shape Prediction

The optimization variables, intrinsic curvature constants and the initial rod deformation, are constant over the length of the needle in shape-sensing. In determining these variables, FBG sensors are indispensable. To predict the shape of the needle further inserted, we must investigate the dependence of the optimization variables on varying insertion lengths. For practical purposes, given a determined shape at a reference insertion length L_{ref} , we aim to predict the shape at a given insertion length L . In order to provide a simple, yet effective approach for accurate predictions, we propose the following form for predicting κ_c for increased insertion lengths

$$\kappa_c(L) = \kappa_{c,ref} (L_{ref}/L)^p, \quad (2)$$

where $\kappa_{c,ref}$ is the optimized κ_c parameter at the insertion length L_{ref} and p is the scaling parameter to be optimized. For flexibility in multi-layer insertion scenarios, we propose using (2) for all κ_c parameters associated with each layer using a single, optimized value of p . This claim is verified by modeling distributed loading forces on an inextensible elastic rod for varying lengths as shown in Section III-A. Then with the similar scaling form of the initial deformation, ω_{init} , needle shape prediction is performed, as explained in Section III-B.

III. THE EXPERIMENT / SIMULATIONS

A. Modeling Inextensible Elastic Rod

Note that the intrinsic curvature includes the external effects for the bending of the needle. Hence in order to investigate the intrinsic curvature constant, we need to solve the equations for an inextensible rod. This rod theory [12] has been successfully applied to cables and double-stranded DNA [13]. Here we assume the needle insertion as a quasi-static process. Necessary rod equations are written as

$$\frac{d}{ds} (B\omega) + \omega \times (B\omega) + \mathbf{e}_3 \times \mathbf{f} = \mathbf{0} \quad (3)$$

$$\frac{d\mathbf{f}}{ds} + \omega \times \mathbf{f} = -\mathbf{f}_{ext} \quad (4)$$

where B denotes the stiffness matrix. $\mathbf{f}(s)$ and $\mathbf{f}_{ext}(s)$ respectively denote the internal force distribution and external force distribution along the needle. For an ideal needle insertion into homogeneous phantom tissue (single bend), $\mathbf{f}_{ext} = [0, -f_n, -f_t]^T$ where f_n and f_t denotes the normal and tangential (or frictional) force densities, respectively. Then we solve (3) and (4) by optimization with the cost function $\mathcal{F} = \|\omega(L)\|^2 + \|\mathbf{f}(L)\|^2 + \|\omega(0) - B^{-1}\mathbf{m}_t\|^2 + \|\mathbf{f}(0) - \mathbf{f}_t\|^2$ where \mathbf{m}_t and \mathbf{f}_t respectively denote the total moment and force applied to the rod. Each term corresponds to a boundary condition: zero moments and forces at the distal end, and balance of moments and forces at the proximal end.

In solving the rod equations (3) and (4) using the distributed loading tangential and normal forces, f_t and f_n , respectively we proposed using a scaling of distributed force densities as

$$f_n = f_{n,ref} (L_{ref}/L)^\nu; f_t = f_{t,ref} (L_{ref}/L)^\nu, \quad (5)$$

where L_{ref} is the reference length to be modeled, and ν is an optimized parameter. The primary assumption associated with ideal insertion of a flexible needle is that the shape from $s \in [0, L_{ref}]$ for the predicted shape will be approximately the same as the reference shape (i.e. the needle follows the path created from its previous insertion). For two-layer cases, we consider (5) for individual layers, requiring ν_1 and ν_2 to optimize.

In order to generate valid predicted insertions, we propose the following optimization problem. Given a series of rod shapes associated with insertion lengths, we define a cost, C_{area} , as the mean pair-wise surface area between rod shapes. Secondly, we define a cost on tip deviation C_{tip} , that is the mean of the pair-wise tip deviation between rod shapes. Finally, the cost function to be minimized is $C = C_{area} + C_{tip}$ where we optimize ν in the force scaling. The cost function is intended to minimize the deviation for further insertion of a flexible needle, as per our assumption of ideal needle insertion. Note that this cost function is used for all optimizations in this paper, including the value p in (2).

B. ω_{init} Scaling and Shape Prediction

For ideal insertions, we have that the initial condition for integrating the E-P equation, $\omega_{init} = \omega_0 = [\kappa_0, 0, 0]^T$, would require a scaling of the same form as (2) with the same value of p . However, in order to account for real-world insertion experiments, we propose a similar, but individual scaling of ω_{init} :

$$\omega_{init}(L) = \omega_{init,ref} (L_{ref}/L)^q \quad (6)$$

where q is a non-universal, optimized parameter. To allow for complex variation in shape, we use q as a separate, optimized parameter per L_{ref} as opposed to p , predicted to be a single, universal value. Finally, with the scaled initial rod deformation, needle shape prediction is performed simply by integrating the E-P equation with scaled κ_c 's using a single parameter p .

Due to limited access to experimental research during the COVID-19 pandemic, we utilize previous single- and double-layer insertion data taken from [7] for needle shape prediction. We simulate needle shapes of increasing insertion lengths and minimize the cost C for the set of shapes through optimizing q in (6). Upon generating the optimized shapes, we perform a workspace analysis through the rotation of the angular deviation vectors, ω and ω_0 , around its body-fixed z -axis in (1). For q optimization, we simulated shapes from the reference length in our data, 90 mm, up to 150 mm in increments of 15 mm.

IV. RESULTS

A. Rod Simulation Results

First, we perform a modeling of the uniformly-distributed loading on an elastic rod with increasing lengths considered, as

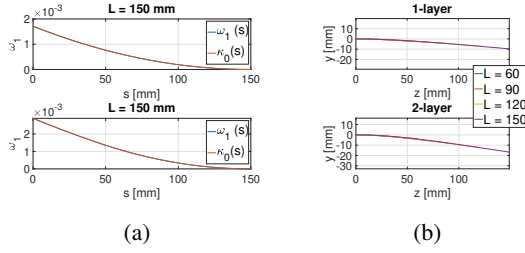


Fig. 2: Upper two panels correspond to single-layer, and lower two panels to double-layer tissue. (a) Comparison between rod deformation and the model for a selected case. (b) Rod configuration from solving the rod equations.

explained in Section III-A. We considered various values of f_n and f_t . Fig. 2(a) shows the comparison of rod deformation obtained from the simulation and the proposed form in the model. This delivers two important conclusions: 1) validity of the proposed form of the intrinsic curvature; and 2) the overlapped rod shapes are all in excellent agreements in various insertion lengths with (5) (Fig. 2(b)). Importantly, when we extracted the relationship between κ_c 's and the insertion lengths L 's ($\kappa_{c,i} \sim L^{-n_i}$, $i = 1, 2$) in two-layer insertion cases, we could find that n_1 and n_2 are reasonably close to each other (e.g., $n_1 \approx 0.65$, $n_2 \approx 0.66$ when $f_n^{(1)} = 0.01$ N/mm, $f_t^{(1)} = 0.003$ N/mm, and $f_n^{(2)} = 0.02$ N/mm, $f_t^{(2)} = 0.006$ N/mm), which strongly supports the proposed scaling form as in (2).

B. Optimization of Scaling on κ_c

Since (2) is confirmed, to determine a universal value of p for the scaling of κ_c , we performed an optimization on p for both single- and double-layer cases that minimizes the sum of errors from each case. As a result, we obtained that value of $p = 0.592$ is the best fit.

C. Needle Prediction

TABLE I: Summary of errors for the single- and double-layer insertion scenarios over the 10 data trials for different calibration methods in [7].

	Calibration	C (mm ²)	Avg. Deviation (mm)
Single-Layer	Jig	12.60 \pm 1.73	0.093 \pm 0.013
	Beam	14.81 \pm 1.92	0.110 \pm 0.014
Double-Layer	Jig	22.77 \pm 6.25	0.169 \pm 0.046
	Beam	22.41 \pm 3.69	0.166 \pm 0.027

By using the method in Section III-B, we can predict 3D shapes from single-layer 90 mm insertion data [7] as seen in Fig. 3. As seen in Table I, we achieved a very low-deviated area error between each pair of predicted needle shapes of 12.60 mm² for jig and 14.81 mm² for beam calibration, thus resulting in average deviations of 0.093 mm and 0.110 mm, respectively, along the needle shaft (for jig and beam calibration methods, see [7]). We predict 3D shapes with low deviation errors by applying the method to the double-layer case presented in [7]. As seen in Fig. 4 and Table I, we achieve an error of 22.77 mm² for jig and 22.41 mm²

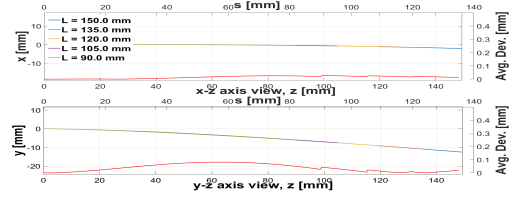


Fig. 3: Predicted needle shapes and deviation error in single-layer tissue from xz - and yz -plane views. Average deviation is 0.093 mm.

for beam calibration, indicating average deviations along the needle shaft of 0.169 mm and 0.166 mm, respectively. Finally,

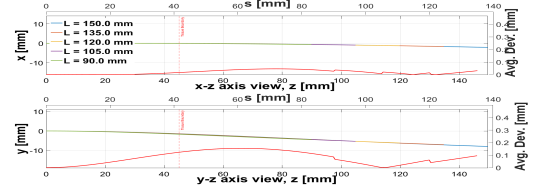


Fig. 4: Predicted needle shapes and deviation error in double-layer tissue from xz - and yz -plane views. Average deviation is 0.166 mm.

after performing the optimization on q for these sets of data, we developed the workspace generated from the single- and double-layer scenarios by allowing for rotations around the z -axis of the needle, as if the operator stopped insertion at 90 mm, and then rotate the needle, and then re-insert the needle. Fig. 5 illustrates the potential workspace from these rotations beginning from a 90-mm insertion predicted to a 150-mm insertion.

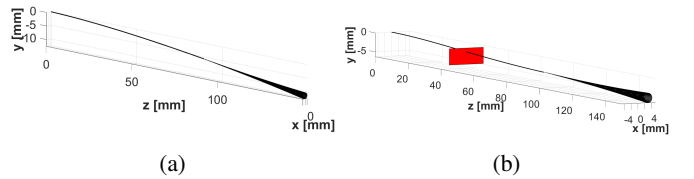


Fig. 5: 3-D workspace generated from needle prediction for (a) single-layer and (b) double-layer insertion scenarios at 150 mm. The red surface denotes the tissue boundary.

V. CONCLUSION

We presented and evaluated a method for needle shape prediction in single- and double-layer tissue insertion generated from previous data. This work is important for extending to more diverse multi-layer insertion scenarios. The presented model accurately predicts the needle shape over large insertion distances and is able to predict the workspace of the needle for further insertions and the potential to be extended into needle motion planning. Experimental validation through insertion experiments and consideration of double-bending, diverse multi-layer scenarios form our future research effort.

REFERENCES

- [1] W. Park, J. S. Kim, Y. Zhou, N. J. Cowan, A. M. Okamura, and G. S. Chirikjian, "Diffusion-based motion planning for a nonholonomic flexible needle model," in *Proceedings of IEEE International Conference on Robotics and Automation*, 2005, pp. 4600–4605.
- [2] R. J. Webster III, J. S. Kim, N. J. Cowan, G. S. Chirikjian, and A. M. Okamura, "Nonholonomic modeling of needle steering," *Int. J. of Robot. Res.*, vol. 25, no. 5–6, pp. 509–525, 2006.
- [3] R. Secoli and F. Rodriguez y Baena, "Closed-loop 3d motion modeling and control of a steerable needle for soft tissue surgery," in *2013 IEEE International Conference on Robotics and Automation*, 2013, pp. 5831–5836.
- [4] M. Khadem, B. Fallahi, C. Rossa, R. S. Sloboda, N. Usmani, and M. Tavakoli, "A mechanics-based model for simulation and control of flexible needle insertion in soft tissue," in *Proceedings of IEEE International Conference on Robotics and Automation (ICRA)*, Seattle, Washington, May 26–30 2015, pp. 2264–2269.
- [5] M. Khadem, C. Rossa, N. Usmani, R. S. Sloboda, and M. Tavakoli, "A two-body rigid/flexible model of needle steering dynamics in soft tissue," *IEEE/ASME Transactions on Mechatronics*, vol. 21, no. 5, pp. 2352–2364, 2016.
- [6] S. Jiang and X. Wang, "Mechanics-Based Interactive Modeling for Medical Flexible Needle Insertion in Consideration of Nonlinear Factors," *Journal of Computational and Nonlinear Dynamics*, vol. 11, no. 1, 01 2016, 011004. [Online]. Available: <https://doi.org/10.1115/1.4030747>
- [7] J. Kim, J. Guo, M. Chatrasingh, S. Kim, and I. Iordachita, "Shape determination during needle insertion with curvature measurements," in *IEEE/RSJ International Conference on Intelligent Robots and Systems (IROS)*, 2017.
- [8] J. S. Kim, M. Chatrasingh, S. Kim, J. Suthakorn, and I. I. Iordachita, "Fiber Bragg Grating based needle shape sensing for needle steering system: Evaluation in inhomogeneous tissue," *Proceedings of IEEE Sensors*, vol. 2017-Decem, no. c, pp. 1–3, 2017.
- [9] G. Chirikjian and A. Kyatkin, *Harmonic Analysis for Engineers and Applied Scientists*. Dover, September 2015, (updated and expanded version of Engineering Applications of Noncommutative Harmonic Analysis, CRC Press, October 2000.).
- [10] D. D. Holm, J. E. Marsden, and T. S. Ratiu, "The Euler-Poincaré equations and semidirect products with applications to continuum theories," *Advances in Mathematics*, vol. 137, pp. 1–81, 1998.
- [11] J. S. Kim and G. S. Chirikjian, "Conformational analysis of stiff chiral polymers with end-constraints," *Molecular Simulation*, vol. 32, pp. 1139 – 1154, 2006.
- [12] S. S. Antman, *Nonlinear Problems of Elasticity*. Springer, 2005.
- [13] S. Goyal, N. Perkins, and C. Lee, "Nonlinear dynamics and loop formation in Kirchhoff rods with implications to the mechanics of DNA and cables," *Journal of Computational Physics*, vol. 209, pp. 371–389, 2005.